



Corrosion of a Nickel-Based Alumina-Forming Alloy in Molten NaCl–MgCl₂ at 600 °C For the Development of a Molten Salt Nuclear Reactor

Louis Pellicot^{1,2} · Nathalie Gruet² · Jérôme Serp³ · Romain Malacarne² · Sophie Bosonnet² · Gaëtan Touze² · Justyna Grzonka⁴ · Laure Martinelli²

Received: 4 July 2024 / Revised: 4 July 2024 / Accepted: 17 July 2024
© The Author(s) 2024

Abstract

Molten chloride salts represent a very corrosive medium due to the amount of impurities they contain and that essentially comes from moisture. In this work, an industrial nickel-based alumina-forming alloy was preoxidized and corroded for 500 h in the NaCl–MgCl₂ eutectic. Electrochemistry and SEM analyses were used to prepare and analyse the corrosion test. Both the nickel-rich matrix and the alumina scale formed during preoxidation seemed to remain stable during the corrosion test contrary to some of the chromium carbides initially present in the columnar microstructure of the alloy. The use of X-ray tomography coupled with SEM observation revealed a preferential dissolution of the chromium carbides connected to the alloy/salt interface. X-ray tomography reveals a chromium carbides network enabling a deep molten salt infiltration within the alloy due to their preferential dissolution. Molten salt infiltration in the dissolved carbides network then leads to the oxidation of aluminium present in the alloy into a mixed MgAl₂O₄ spinel. An oxoacido-basic reaction between the alumina scale formed at the alloy surface during preoxidation and MgO dissolved in the salt is also discussed. This work shows that nickel-based alumina-forming alloy present a realistic interest and that the microstructure of the alloy should be optimized in further work to enhance corrosion resistance.

Keywords Corrosion · Molten chloride salts · Nickel-based alumina-forming alloy · Electrochemical techniques · X-ray tomography

Introduction

Over the last decade, molten chloride salts have been considered as a heat-transfer fluid in various power-plants as they allow a better efficiency than water at atmospheric pressure [1, 2]. Concentrating solar plant or molten salt reactors (MSR)

Extended author information available on the last page of the article

can be cited as examples. In the case of a MSR, the molten salt would contain uranium or plutonium chloride added to a NaCl–MgCl₂ base salt [2]. However, conventional material cannot withstand the high corrosiveness of molten chloride salts and more specifically of NaCl–MgCl₂ [3–7]. This is a consequence of the impurities present in the salt (essentially moisture and oxides ions) due to the strong hygroscopy of MgCl₂ as shown by Mortazavi et al. [8, 9]. In general, corrosion of alloys in molten NaCl–MgCl₂ is due to a preferential dissolution of chromium and iron that leads either to general corrosion or to intergranular corrosion [8, 10–12]. Intergranular corrosion is often observed when chromium carbides are present at the grain boundaries [11]. The solubility of chromium in molten chloride salts prevents chromia-forming alloy from forming a protective oxide scale as Cr₂O₃ soluble in molten chloride salts as shown by Ishitsuka et al. [13]. Ding et al. have also shown that alumina-forming alloys performed better than chromia-forming alloys in NaCl–MgCl₂–KCl at 700 °C [14]. Therefore, alumina-forming alloy could be a solution to the corrosion problem in this medium. Some of these alloys were studied but their preoxidation did not allow to grow a protective alumina scale on them [15, 16]. In this work, Manaurite XA14[®] provided by Manoir Industries was preoxidized and immersed for 500 h at 600 °C in molten NaCl–MgCl₂ eutectic (0.57 mol frac. NaCl–0.43 mol frac. MgCl₂ or 0.45 wt frac. NaCl–0.55 wt frac. MgCl₂). As nickel-based alloy have better corrosion resistance in molten chlorides salts than steel, and as chromia is highly soluble in molten chlorides, a nickel-based alumina-forming alloy is considered in this study. The XA14 alloy, provided by Manoir Industries, is a nickel-based alumina-forming alloy already produced at an industrial scale, which is an asset in the perspective of building a MSR prototype. Moreover, the effect of Cr carbides is discussed in chromia-forming alloys [17–19] and the presence of high content of C in XA14 is an advantage to study the effect of Cr carbides in alumina-forming alloys. For these reasons, the corrosion of the XA14 alloy has been investigated in this study.

Materials and Methods

The molten NaCl–MgCl₂ was prepared from NaCl provided by Sigma-Aldrich with a 99.9% purity and MgCl₂ provided by Acros international with a 99% purity. The salts were mixed to reach the eutectic composition. The salts were stored and mixed in a glovebox under pure argon (< 10 ppm vol O₂ and < 20 ppm vol H₂O), and the whole experiment (purification of the salt, corrosion test) was performed inside the glovebox. The salt was first dehydrated at 120 °C for 48 h in a quartz crucible inserted inside a closed reactor under sweeping high-purity argon (99.99999% vol Ar). It was then melted at 600 °C and kept under Ar sweeping for 12 days in order to wait for the magnesium hydroxychlorides decomposition into MgO. Magnesium oxide has a low solubility limit in NaCl–MgCl₂ melts and precipitate at the bottom of the crucible [9, 20, 21]. As MgO precipitates

(shown by X-ray diffraction made on purified salt, not shown here), the salt is saturated in oxide ions.

To check the oxide content of the salt, cyclic voltammetry (CV) was used (Fig. 1). The working and counter electrodes were pure tungsten wires provided by Goodfellow. The electrodes surface was 0.33 cm^2 and the sweep rate was 100 mV/s . The reference electrode Ag/AgCl was custom-made using a silver wire provided by Thermochemical immersed in a 0.54 mol frac. NaCl-0.40 mol frac. MgCl_2 - 0.06 mol frac. AgCl salt contained in a pyrex immersion sleeve. All electrochemical experiments were performed using a SP-200 potentiostat (Biologic) controlled by an EClab software v11.43. The voltammograms were traced 5 times and the 4th cycle was used for representation. The CV graphs were then plotted so that the Cl^-/Cl_2 wall began at 0 V. A tangent to the oxidation signal of Cl^- is drawn in the part where the current density is greater than 100 mA/cm^2 . The voltammogram is then displaced so that the tangent intersects the abscissa axis at 0 V. This process enables different CVs to be compared despite the possible use of other reference electrodes. The non-superimposition of the Mg/Mg^{2+} ($E \approx -2.75 \text{ V}$ in Fig. 1) wall can be observed and is a consequence of variations in salt composition during the experiment. The salt is considered sufficiently purified when the peaks of oxides (between -1 V and -0.5 V vs Cl^-/Cl_2 , Fig. 1a) and hydroxychlorides (plateau at $E < -1.5 \text{ V}$ vs Cl^-/Cl_2 in Fig. 1a) reach an absolute current density value inferior to 10 mA/cm^2 (Fig. 1b) [22]. In that case, it is considered that the salt is only saturated with oxide ions (but not oversaturated) and free of hydroxychlorides.

The material used was Manaurite XA14[®] provided by Manoir Industries. The composition is 22–27 wt% Cr, 3.5–4.5 wt% Al, 18–30 wt% Fe, 0.4–0.5 wt% C and Ni is in balance. The coupons were preoxidized at $950 \text{ }^\circ\text{C}$ under dry air for 24 h with a $120 \text{ }^\circ\text{C/h}$ heating rate and immersed for 500 h at $600 \text{ }^\circ\text{C}$ in liquid NaCl– MgCl_2 . Open-circuit potential of the sample was measured during the corrosion test.

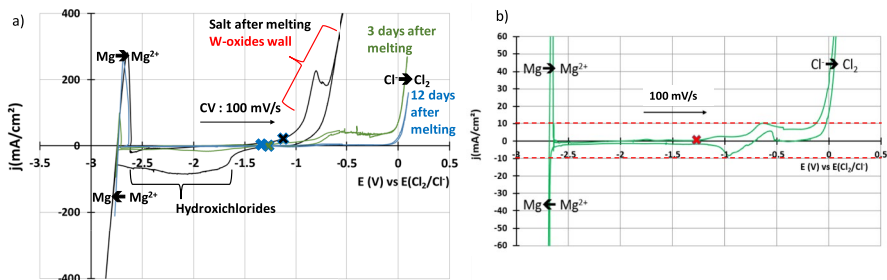


Fig. 1 **a** j - E curves obtained by cyclic voltammetry of NaCl– MgCl_2 during purification process. The black curve corresponds to the salt after melting (the oxide peak is observed at $E = -1 \text{ V}$ vs $E_{\text{Cl}_2/\text{Cl}^-}$ and the hydroxychlorides plateau at $E < -1.5 \text{ V}$ vs $E_{\text{Cl}_2/\text{Cl}^-}$), the green curve corresponds to 3 days after melting (the oxide peak is observed at $E = -0.5 \text{ V}$ vs $E_{\text{Cl}_2/\text{Cl}^-}$ and the hydroxychlorides peak has disappeared) and the blue one to 12 days after melting (the oxide and the hydroxychlorides peaks have almost disappeared). **b** j - E curve of NaCl– MgCl_2 before corrosion test. Crosses correspond to the open-circuit potential of each salt measured after 1 h at rest (Color figure online)

The alloy microstructure is composed of a FCC Ni base matrix containing in solid solution Cr, Fe and Al. A network of chromium carbides is detected by X-ray tomography (Fig. 2a) and is coloured in purple, they are present along the grain boundaries but also across a few grains. The chromium carbides appear bigger than what they are in reality due the tomography post-treatment process. However, as some smaller carbides are not detected by the X-ray tomography, the calculated volume fractions of carbides, performed by the X-ray Tomography software, is 0.18 for Cr carbides and 0.018 for Nb carbides. They are in agreement with TCNi12 calculations (0.2 volume fraction for all carbides) provided by Manoir Industries. (Nb-Ti)C precipitates are also present in the alloy [23, 24] and are coloured in green in Fig. 2b. The microstructure of the alloy is columnar due to the centrifugal casting technique used to produce the material [24]. As cast, the chromium carbides present have a M_7C_3 stoichiometry but will transform at 600 °C into $M_{23}C_6$ according to Roussel et al. [25].

XAl4 coupons were hanged using a silver wire and half-immersed in the salt. The salt was analysed by ICP-AES after the corrosion test.

After the corrosion test, the part of the coupon immersed in the molten salts was cut using an Owell wire saw with kerosene product as a lubricant to avoid dissolution of water-soluble species. Hitachi IM5000 Ar Ion Beam Milling System was used to polish the cross sections for SEM observations carried out using a Zeiss Gemini Ultra 55 SEM coupled with a Bruker X-Flash[®] EDS-X detector and a Hitachi SU8700 equipped with an Oxford UltimMax100 EDS-X system with a 15 keV voltage. X-ray tomography was realized on a Phoenix VtomeX m form Waygate Technologies. A 240 kV reflexion tube and a 180 kV transmission tube were used with a 130 kV tension and a 20 μ A current. A 0.5 mm Al filter was used. The size of a voxel is 1.7 μ m. 2200 images were made. There are no scale on the X-ray tomography pictures because it would not be exact due to perspective on the pictures.

Fluorescence spectroscopy on preoxidized alloys was performed using a HORIBA LabRam HR800 with 532 nm laser.

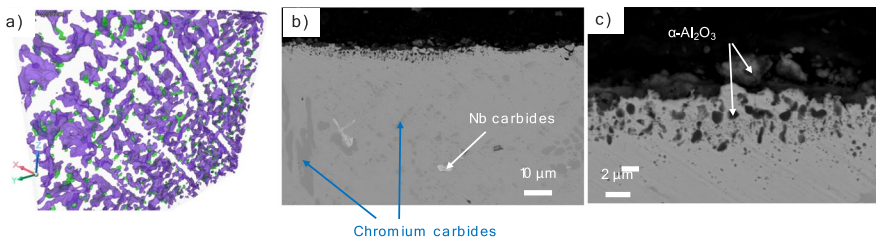


Fig. 2 Micrographies of the XAl4 after preoxidation. **a** X-ray tomography Cr carbides represented in purple and Nb-Ti carbides in green. **b** and **c** SEM-BSE cross sections (higher magnification for **c**) (Color figure online)

Results

XAl4 Microstructure and Preoxidation

The microstructure of the preoxidized alloy, shown in Fig. 2, is composed of chromium carbides in the matrix and an oxide at the top of the sample.

After preoxidation, SEM-EDS-X and fluorescence spectroscopy were used to identify the oxide scale. It contains Al and O according to EDS-X analyses. As shown in Fig. 3, the Cr^{3+} ions fluorescence spectrum observed confirmed the presence of α -alumina on top of the alloy. Indeed, fluorescence of Cr^{3+} dopant can be used to identify α -alumina [26]. SEM observation showed that this alumina scale was about 1 μm thick. Some alumina precipitates are also observed underneath the alloy surface.

Salt After Corrosion

At the end of the corrosion test, the molten salt was analysed using cyclic voltammetry (CV) on a W working electrode. The CV curves is represented in orange in Fig. 4a. The potential of the salt measured by open circuit on the W working electrode is -1.33 V versus $E_{\text{Cl}_2/\text{Cl}^-}$. Between the reduction in Mg^{2+} and the oxidation of Cl^- , three peaks are observed: one corresponding to the oxide ions oxidation (at -0.5 V versus $E_{\text{Cl}_2/\text{Cl}^-}$), one corresponding to reduction of hydroxychlorides (plateau at $E < -2$ V versus $E_{\text{Cl}_2/\text{Cl}^-}$) and the last one at $E \approx -1.7$ V versus $E_{\text{Cl}_2/\text{Cl}^-}$ in Fig. 4a. In order to identify the species corresponding to this last anodic peak, a voltammogram was carried out on a salt containing 4.10^{-3} mol/L of CrCl_2 (blue curve in Fig. 4a). This voltammogram shows that the Cr/Cr^{2+} redox couple is indeed in the $[-2; -1.8]$ V versus $E_{\text{Cl}_2/\text{Cl}^-}$ potential interval. The last peak observed on the salt after corrosion (orange curve, Fig. 4a) is therefore attributable to the Cr/Cr^{2+}

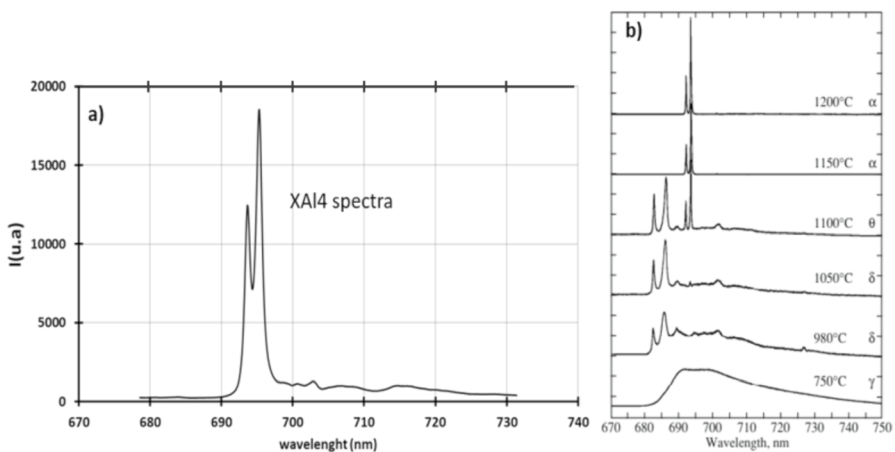


Fig. 3 **a** Fluorescence spectrum of preoxidized XAl4, **b** fluorescence spectra of various allotropic forms of alumina according to Kulinkin et al. [21]

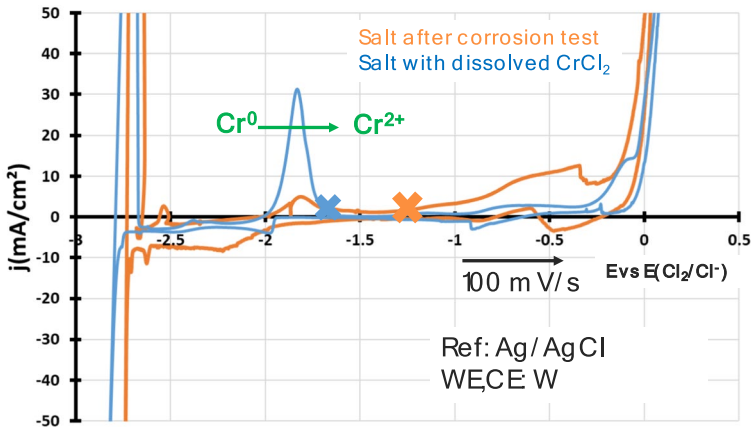


Fig. 4 CV performed on W working electrode after the corrosion test (orange curve) and in a salt containing 4.10^{-3} mol/L of CrCl_2 (blue curve): the oxidation peak of Cr^0 into Cr^{2+} is measured at about -1.7 V versus $E_{\text{Cl}_2/\text{Cl}^-}$. Crosses correspond to the open-circuit potential of each salt measured after 1 h at rest (Color figure online)

couple: Cr dissolution occurred during the corrosion test leading to the presence of Cr^{2+} dissolved in the salt. ICP-AES analysis was performed on a salt sample (sample was taken at 600 °C) after the corrosion test. Cr, Ni, Fe and Al concentration given by the ICP-AES analysis were respectively: 2.10^{-4} mol/L and values inferior to 3.10^{-5} mol/L. No iron nor nickel nor aluminium can be observed on the CV in Fig. 4a, showing preferential dissolution of Cr into Cr^{2+} .

Microstructure After Corrosion

During the corrosion test, the potential of the XAl4 coupon is measured and equal to about -1.7 V versus $E_{\text{Cl}_2/\text{Cl}^-}$.

After corrosion test, the alloy was observed by SEM and X-ray tomography and analysed on cross section using EDS-X (Fig. 5, 6, 7, 8, 9). As shown in Fig. 5, the corrosion is both external and internal. The matrix does not seem to corrode. At the sample/salt interface, the alumina scale is still present (Fig. 6, 7).

At the alloy/salt interface, the oxide scale was analysed using EDS-X (Fig. 6). As shown in Fig. 6, a mixed Mg–Cr oxide surrounds the alumina scale. EDS-X analyses of the mixed oxide show that Mg/Al/O ratios correspond to MgAl_2O_4 , which probably forms from the reaction between alumina and MgO dissolved in the salt. The thickness of the alumina scale was approximately 2 μm before the corrosion test. After 500 h of immersion, it was slightly superior to 2 μm as shown in Fig. 7 as MgO and Al_2O_3 begun to react to form MgAl_2O_4 . The thickness of the MgAl_2O_4 oxide scale is approximately 3 μm after 1000 h of immersion test. This variation can be attributed to the oxide transformation from Al_2O_3 to MgAl_2O_4 as MgAl_2O_4 molar volume is 1.53 times greater than Al_2O_3 molar volume. The alumina scale formed during preoxidation seems to be a temporary

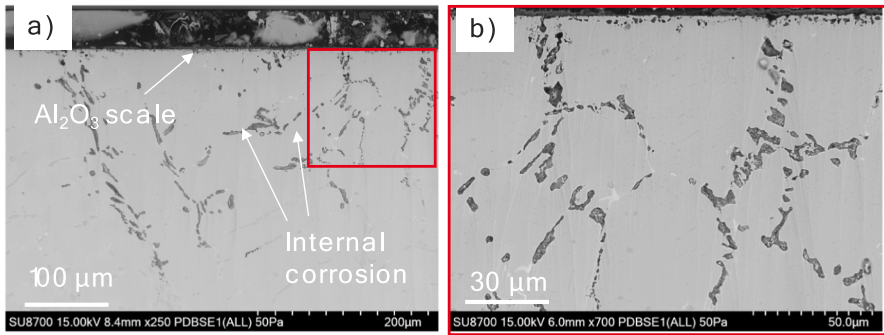


Fig. 5 SEM observation on cross section of the corroded XA14: **a** overview, **b** higher magnification

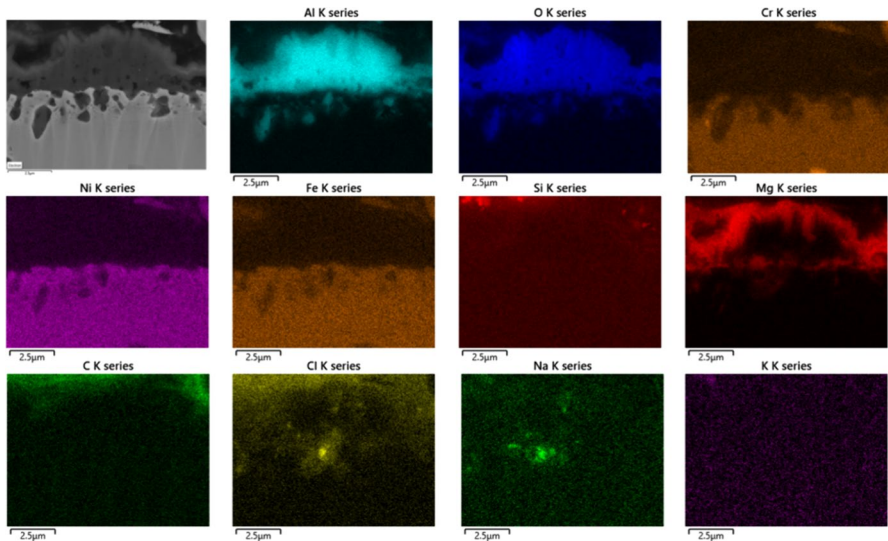


Fig. 6 SEM cross-section picture and elemental SEM-EDS-X mapping of the oxide scale at the XA14 / salt interface

barrier to the salt corrosion but does not seem to grow during corrosion. No chromium depletion is observed beneath the oxide (Fig. 6, 8). The alumina precipitates underneath the surface during the preoxidation seem to be stable as they are still observed in Fig. 6. Their size, amount and distribution are approximately the same as the ones just after preoxidation.

The internal precipitates depth is approximately 100 μm (Fig. 5). As shown in Fig. 8, this internal precipitation is mainly intergranular and correspond to enrichment of Al–O–Mg–Na–Cl.

The presence of chlorine and sodium is the indication of salt infiltration into the material. Strong chromium depletion can be observed near the internal

Fig. 7 SEM-BSE picture of cross section of XAl4 corroded 500 h at 600 °C in liquid NaCl–MgCl₂ eutectic

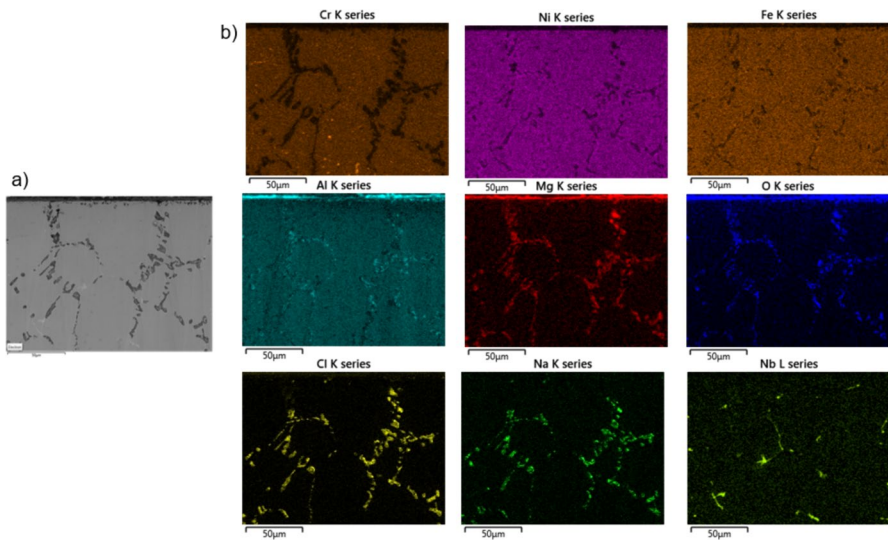
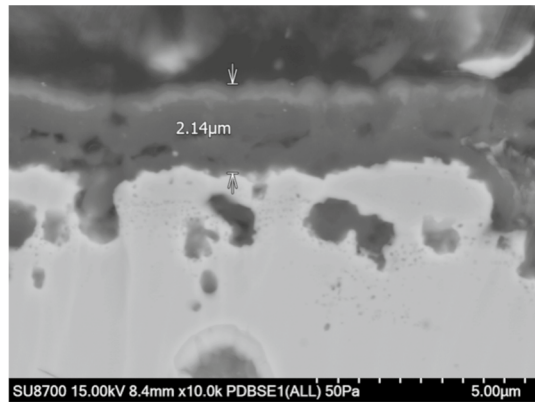


Fig. 8 **a** SEM cross-section micrography and **b** elemental EDS-X mapping of the corroded XAl4

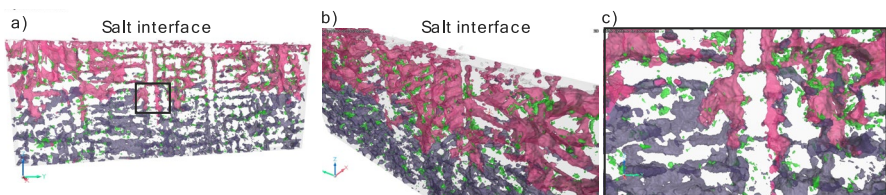


Fig. 9 X-ray tomography picture of the precipitates in the corroded XAl4. MgAl₂O₄ spinel precipitates appear in pink, Cr carbides in purple and Nb carbides in green. **a** cross section of the alloy **b** top view of the alloy/salt interface, **c** zoom in the black square in cross section (**a**) (Color figure online)

precipitates. Cr preferential dissolution revealed by ICP-AES analyses is therefore a localized corrosion process.

SEM-EDS-X quantitative analysis of the internal precipitates are presented in Table 1. They were realized with a 15 keV acceleration voltage and quantified using a standard library implemented during preliminary work. The Al/Mg/O ratios are close to the MgAl_2O_4 spinel and Na and Cl are present in small amount (here Cl is not detected but other spots showed the presence of small amount of Cl). Note that the quantification of Na by EDS-X is not reliable because of the instability of Na atoms under electron beam.

X-ray tomography was used to analyse the carbides network within the alloy after corrosion. In Fig. 9, the MgAl_2O_4 precipitates are represented in pink, the chromium carbides in purple and the Nb carbides in green. Comparing Fig. 2 and Fig. 9, the Nb carbides appear to remain stable during the corrosion test. However, the Cr carbides have completely disappeared just below the alloy/salt interface where the MgAl_2O_4 precipitates are located. Moreover, Fig. 9 reveals a continuity between the MgAl_2O_4 precipitates and the carbide network. This figure also shows that the MgAl_2O_4 precipitates network is linked to the surface of the alloy.

Discussion

To understand the corrosion behaviour of metal or alloys in molten salt, $E\text{-}p\text{O}^{2-}$ diagram can be drawn upon the model of Pourbaix's diagram. The pH is replaced by the activity of oxide anions represented in this case by MgO as O^{2-} is not implemented in thermodynamics database. Figures 10 and 11 represent the diagram of chromium, aluminium and nickel calculated with HSC 7.1 database [27]. In Fig. 10, the full black lines represent the diagrams where all activities equal 1 and the dotted blue lines represent the diagrams where the activity of dissolved elements equal 0.0001 for chromium (that corresponds to the dissolved Cr concentration measured in the molten salt) and 0.00001 for Al. For the dotted blue lines, the activity of metallic elements equals their activity in the alloy calculated by Thermocalc at 600 °C using TCFE8 database, which are $1.4 \cdot 10^{-7}$ for Al and 0.93 for Cr. All other activities equal 1. In Fig. 11, no soluble specie is stable, the activity of NiO is equal to 1 and the activity considered for Ni is its activity in the alloy, calculated by Thermocalc and equal to 0.65. Activity of MgCl_2 and Cl^- are equal to their molar fraction value according to Delpech et al.: 0.5 for Cl^- and 0.45 for MgCl_2 [27]. The experimental salt potential, measured on the W electrode is represented by the orange line in the 3 diagrams. The red cross, in the 3 diagrams, corresponds to the couple [MgO

Table 1 Quantitative analysis (EDS-X) of an internal precipitate. The sum, indicated in wt%, (as in mol %, the sum is normalized at 100%) is given to permit the assessment of the quantification quality

Element	O	Na	Mg	Al	Cl	Cr	Fe	Ni	Sum (wt%)
Mol%	44.5	0.3	17.9	27.9	0.0	0.6	2.8	5.9	96

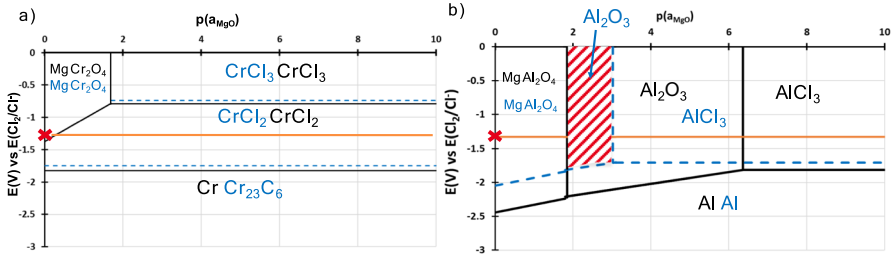


Fig. 10 E - $p(a_{\text{MgO}})$ diagrams of chromium (a) and aluminium (b) at 600 °C calculated using HSC 7.1 database. The full black lines correspond to all activity (solid and solutes) equal to 1. The dotted blue lines correspond to dissolved Cr and Al chlorides activities equal to the Cr and Al concentrations measured by ICP-AES in the salt (10^{-4} for Cr and 10^{-5} for Al) and Cr and Al activities equal to their activities in the alloy calculated by Thermocalc at 600 °C (0.93 for Cr and $1.4 \cdot 10^{-7}$ for Al). Orange line is the experimental salt potential (measured on W electrode). The red cross corresponds to the couple [MgO activity, salt potential] in the salt. The Al_2O_3 domain has been hatched in red (Color figure online)

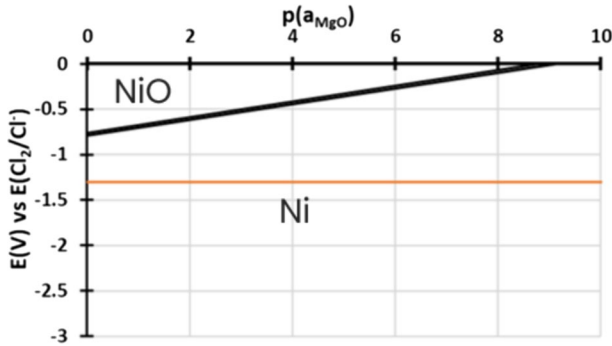


Fig. 11 E - $p(a_{\text{MgO}})$ diagram of nickel at 600 °C calculated using HSC 7.1 database. Activity of Ni is 0.65 (calculated by TCFE8). Orange line is the experimental salt potential (measured on W electrode) (Color figure online)

activity, salt potential]. Activity of MgO is assumed to be 1 as the salt is oxide ions saturated (purification process leads to MgO precipitation as proposed in “Materials and Methods” section). These diagrams are calculated at 600 °C. They show that: (i) Ni is in its immunity domain in the salt conditions represented by the red cross in Fig. 10 and 11 (even whatever the dissolved MgO activity). It explains the absence of dissolved Ni in the salt and the absence of general dissolution of the matrix. (ii) The transformation of Al_2O_3 into MgAl_2O_4 is predictable when there is a high oxide activity as it is the case in this study. (iii) The dissolution of chromium into Cr^{2+} represented as CrCl_2 is also predictable in a large domain that is very close to the immersion conditions (red cross in Fig. 10). There are two possibilities: MgCr_2O_4 forms according to the diagram (the red cross is in its stability domain) and is soluble in the molten salt as MgCr_2O_4 was not observed on our sample; or CrCl_2 is formed even if the test conditions are in the MgCr_2O_4 predominance domain. The predominance of MgCr_2O_4 predicted by on the basis of a thermodynamic calculation

does not imply an absence of CrCl_2 . Kinetic competition favouring the dissolution of Cr in CrCl_2 over its oxidation into MgCr_2O_4 could explain the presence of dissolved Cr in the salt and the absence of MgCr_2O_4 formation as internal precipitates. Figure 10 also shows that oxidation potentials of Cr^0 into Cr^{2+} and Cr_{23}C_6 into Cr^{2+} are very close which explains the preferential oxidation of Cr carbides (corresponding to a Cr reservoir) and Cr from the matrix surrounding the Cr carbides.

A large domain of stability exists for Al_2O_3 and has been hatched in red in Fig. 10b. It corresponds to a rather low activity of MgO and high potential condition. To have a stable alumina scale on the material, the alloy should be placed in this zone. To achieve this objective, working with an unsaturated salt in MgO is necessary. This condition will be very difficult to reach because the saturation value is very low according to literature. Furthermore, this will be even more difficult to meet at an industrial process without adding a getter, where there are many more opportunities for H_2O and O_2 to infiltrate the plant and pollute the salt.

At the alloy/salt interface, the alumina scale reacts with the dissolved MgO to form MgAl_2O_4 . The reaction proposed is:



Reaction (1) is an acido-basic reaction, as Al_2O_3 reacts with the MgO base without changing the oxidation degree of the involved elements.

The MgAl_2O_4 internal precipitates are connected to the surface of the sample, as shown by X-ray tomography in Fig. 9 and salt infiltrates this network as Na–Mg–Cl are deeply present in the intragranular corrosion as shown by EDS-X mapping in Fig. 8. Na and Cl are detected as traces because they are not constitutive of the precipitates, unlike Mg. As a result of all these experimental facts, the following corrosion mechanism can be proposed and is represented in Fig. 12: (i) first, the salt reacts with the sample surface: alumina turns into MgAl_2O_4 by an acido-basic reaction with dissolved MgO (reaction (1)). The chromium carbides that emerge at the surface (Fig. 12a) begin to dissolve in the salt according to Fig. 10a, ICP-AES measurements, CV curves in Fig. 4a, EDS-X analyses in

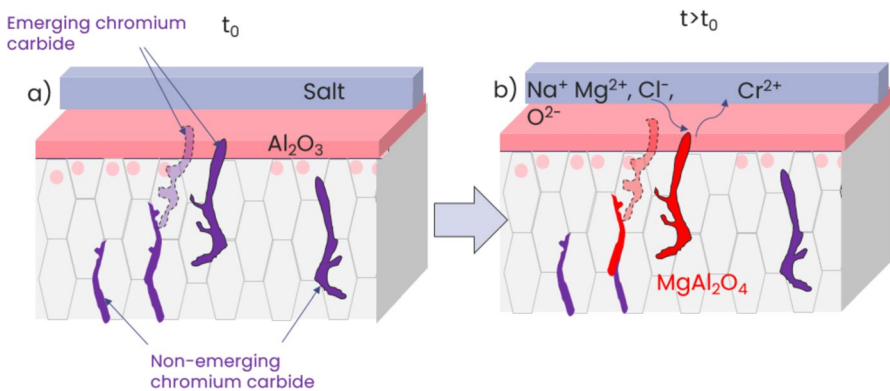


Fig. 12 Diagram of the corrosion process of XAl4 **a** at the beginning, **b** during the corrosion

Fig. 8 and X-ray tomography in Fig. 9. (ii) Then, the salt penetrates in the available space formed by the carbides dissolution. (iii) Mg^{2+} and O^{2-} dissolved in the salt react with the surrounding aluminium (oxidized by the oxidant present in the salt: dissolved H_2O , HCl , O_2 or Cl_2) of the alloy and form the MgAl_2O_4 precipitates in the space left by the dissolution of chromium carbides. Gradually (Fig. 12b), all the carbides emerging on the surface of the alloy dissolve while the salt penetrates this available space and oxidizes aluminium, forming a network of MgAl_2O_4 precipitates in place of the network of chromium carbides. The chromium carbides that are not emerging at the surface do not dissolve. As shown in Fig. 9, the Nb rich carbides do not dissolve in the molten salt. While chromium is dissolving from the carbides, carbon could either dissolve in the surrounding matrix or precipitate at the bottom of the crucible, since carbon is not soluble in molten chlorides salts. However, observations performed do not allow the carbon to be measured precisely, so the carbon dissolution mechanism (in the matrix or in the salt) still needs to be studied.

Conclusion

A nickel-base alloy was preoxidized and immersed in molten NaCl-MgCl_2 eutectic for 500 h at 600 °C. The preoxidation was efficient and a continuous alumina scale was developed the alloy surface. The Ni matrix did not dissolve due to the high nobility of nickel in the molten salt. The alloy corrosion is due to the dissolution of chromium carbides that form a network emerging at the alloy surface. MgAl_2O_4 forms in place of the dissolved carbide, while the alumina scale also transforms into MgAl_2O_4 . These results are consistent with thermodynamic predictions of the E - pO^{2-} diagrams. Al_2O_3 is not as stable as expected and the protectiveness of MgAl_2O_4 should be further investigated. The XAl4 alloy should be improved to eliminate the chromium carbides, which are problematic for corrosion resistance. The alloy's ability to form alumina must be preserved. The carbon can either dissolve in the salt or dissolve in the alloy. In the first case, it is difficult to detect because it is not an electroactive species and it cannot be detected by ICP-AES (analysis carried out at the end of the test on a salt sample). In the second case, it is also difficult to detect by EDS-X. Further investigations are needed to identify the C dissolution mechanism.

Acknowledgements The authors are grateful to Manoir Industries R&D department and head of R&D department Manuel Roussel for providing the material and all the useful information for the realization of this work. They thank France 2030 and Innovative System for Actinides Converter (ISAC) program for funding this project.

Author Contribution Conceptualization was done by L.M. and N.G.; methodology was done by L.M., N.G. and J.S.; validation was done by L.M., N.G., R.M.; investigation was done by L.P., R.M., S.B., L.M., G.T, J.G and N.G.; writing—original draft preparation was done by L.P.; writing—review and editing was done by L.P., R.M., N.G., L.M., J.S.; supervision was done by L.M., N.G. and J.S. All authors reviewed the manuscript.

Data Availability Data can be accessed on demand to authors due to CEA's data policy.

Declarations

Conflict of interest The authors declare no competing interests.

Open Access This article is licensed under a Creative Commons Attribution-NonCommercial-NoDerivatives 4.0 International License, which permits any non-commercial use, sharing, distribution and reproduction in any medium or format, as long as you give appropriate credit to the original author(s) and the source, provide a link to the Creative Commons licence, and indicate if you modified the licensed material. You do not have permission under this licence to share adapted material derived from this article or parts of it. The images or other third party material in this article are included in the article's Creative Commons licence, unless indicated otherwise in a credit line to the material. If material is not included in the article's Creative Commons licence and your intended use is not permitted by statutory regulation or exceeds the permitted use, you will need to obtain permission directly from the copyright holder. To view a copy of this licence, visit <http://creativecommons.org/licenses/by-nc-nd/4.0/>.

References

1. K. Vignarooban, X. Xu, A. Arvay, et al., *Applied Energy* **146**, 2015 (383).
2. J. Serp, M. Allibert, O. Benes, et al., *Progress in Nuclear Energy* **77**, 2014 (308).
3. L. Guo, Q. Liu, H. Yin, et al., *Corrosion Science* **166**, 2020 (108473).
4. W. Junwei, Z. Hongxia, Z. Rongjiang, et al., *Rare Metal Materials and Engineering* **46**, 2017 (935).
5. H. Sun, J. Wang, Z. Li, et al., *Solar Energy* **171**, 2018 (320).
6. S. Liu, Z. Liu, Y. Wang, et al., *Corrosion Science* **83**, 2014 (396).
7. N. S. Patel, V. Pavlík, M. Boča, et al., *Critical Reviews in Solid State and Materials Sciences* **42**, 2017 (83).
8. A. Mortazavi, Y. Zhao, M. Esmaily, et al., *Solar Energy Materials and Solar Cells* **236**, 2022 (111542).
9. G. J. Kipouros and D. R. Sadoway, *Journal of Light Metals* **1**, 2001 (111).
10. O. Muránsky, C. Yang, H. Zhu, et al., *Corrosion Science* **159**, 2019 (108087).
11. B. Grégoire, C. Oskay, T. M. Meißner, et al., *Solar Energy Materials and Solar Cells* **223**, 2021 (110974).
12. A. Chmakoff, PhD thesis, Compréhension des mécanismes de corrosion en environnement réacteurs du futur à combustible et caloporteur sels fondus. Université Paris Saclay (2023).
13. T. Ishitsuka and K. Nose, *Corrosion Science* **44**, 2002 (247).
14. W. Ding, H. Shi, A. Jianu, et al., *Solar Energy Materials and Solar Cells* **193**, 2019 (298).
15. J. C. Gomez-Vidal, A. G. Fernandez, R. Tirawat, et al., *Solar Energy Materials and Solar Cells* **166**, 2017 (234).
16. A. G. Fernández and L. F. Cabeza, *Coatings* **10**, 2020 (138).
17. A. U. Seybolt, *Oxidation of Metals* **2**, 1970 (119).
18. I. Polovov, A. Abramov, O. Rebrin, et al., *ECS Transactions* **33**, 2010 (321).
19. R. Pillai, S. S. Raiman, and B. A. Pint, *Journal of Nuclear Materials* **546**, 2021 (152755).
20. Y. Kirsh, S. Yariv, S. Shoval, et al., *Journal of Thermal Analysis* **32**, 1987 (393).
21. Q. Huang, G. Lu, J. Wang, et al., *Journal of Analytical and Applied Pyrolysis* **91**, 2011 (159).
22. R. A. Skar, H. Mediaas, T. Østvold, et al., *Canadian Metallurgical Quarterly* **43**, 2004 (381).
23. J. Allo, S. Jouen, M. Roussel, et al., *Oxidation of Metals* **95**, 2021 (359).
24. A. Facco, M. Couvrat, D. Magné, et al., *Materials Science and Engineering: A* **783**, 2020 (139276).
25. M. Roussel, X. Sauvage, M. Perez, et al., *Materialia* **4**, 2018 (331).
26. A. B. Kulinkin, S. P. Feofilov, R. I. Zakharchenya, et al., *Physics of the Solid State* **42**, 2000 (857).
27. S. Delpéch, C. Carrière, A. Chmakoff, et al., *Materials* **17**, 2024 (581).

Publisher's Note Springer Nature remains neutral with regard to jurisdictional claims in published maps and institutional affiliations.

Authors and Affiliations

**Louis Pellicot^{1,2} · Nathalie Gruet² · Jérôme Serp³ · Romain Malacarne² ·
Sophie Bosonnet² · Gaëtan Touze² · Justyna Grzonka⁴ · Laure Martinelli²**

✉ Louis Pellicot

louis.pellicot@cea.fr

Nathalie Gruet

nathalie.gruet@cea.fr

Jérôme Serp

jerome.serp@cea.fr

Romain Malacarne

romain.malacarne@cea.fr

Sophie Bosonnet

sophie.bosonnet@cea.fr

Gaëtan Touze

gaetan.touze@cea.fr

Justyna Grzonka

justyna.grzonka.jg@hitachi-hightech.com

Laure Martinelli

laure.martinelli@cea.fr

- ¹ Chimie Physique et Chimie Analytique de Paris-Centre (ED-388), Université Paris Sorbonne, Paris, France
- ² Service de Recherche en Corrosion et Comportement des Matériaux, CEA, Université Paris-Saclay, 91190 Gif-sur-Yvette, France
- ³ DES, ISEC, CEA, DMRC, University of Montpellier, Marcoule, 30 207, Bagnols-sur-Cèze, France
- ⁴ Hitachi High-Tech Europe, GmbH, Europark Fichtenthain A12, 47807 Krefeld, Germany